Modifying Perovskite Films with Polyvinylpyrrolidone for Ambient-Air-Stable Highly Bendable Solar Cells

Hao Xiong[a,b]*, Giovanni DeLuca*[b]*, Yichuan Rui*[c]*, Jiabin Qi*[a]*, Yaogang Li*[a]*, Qinghong Zhang*[a*]*, Hongzhi Wang*[a*] *and Elsa Reichmanis* [b,d*]

[a] State Key Laboratory for Modification of Chemical Fibers and Polymer Materials, College of Materials Science and Engineering, Donghua University, Shanghai 201620, P. R. China

[b] School of Chemistry and Biochemistry, Georgia Institute of Technology, 901 Atlantic Drive, Atlanta, Georgia 30332, United States

[c] College of Chemistry and Chemical Engineering, Shanghai University of Engineering Science, Shanghai 201620, PR China

[d] School of Chemical and Biomolecular Engineering, Georgia Institute of Technology, 311 Ferst Drive NW, Atlanta, Georgia 30332, United States

[*]**Corresponding author:** Tel: +86-21-67792943; Fax: +86-21-67792855. E-mail address: zhangqh@dhu.edu.cn (Q. Zhang), wanghz@dhu.edu.cn (H. Wang), elsa.reichmanis@chbe.gatech.edu (E. Reichmanis).

ABSTRACT

One major drawback that prevents the large-scale practical implementation of perovskites is their susceptibility to performance degradation in humid environments. Here we achieved uniform, stable perovskite films within a polyvinylpyrrolidone (PVP) polymer frame *via* mild solution processing in ambient air with over 60% relative humidity. In addition to facilitating film formation, the hydrophobic PVP served to protect the perovskite grains from atmospheric moisture. Use of PVP, coupled with optimization of the deposition parameters, provided for compact, smooth, pinhole-free perovskite films that when incorporated into a photovoltaic device exhibited highly reproducible efficiencies in the range of up to 17%. In the absence of encapsulation, the devices exhibited stable performance characteristics during exposure to humid ambient air for 600 hours. Furthermore, on flexible substrates, the 8 wt% PVP-perovskite samples provided for device efficiencies of *ca.* 15%. The devices retained *ca.* 73% of their efficiency after bending 1000 times with a bending radius of 0.5 cm.

KEYWORDS: Perovskite solar cells; polymer doping; polyvinylpyrrolidone; flexible solar cells.

1. INTRODUCTION

As certified by the National Renewable Energy Laboratory (NREL), the power conversion efficiency of perovskite solar cells (PSCs) has reached 22.7% when fabricated using an optimized device architecture.[1] The dramatic improvements that led to such high efficiencies were due to the excellent semiconductor properties of ABX_3 perovskite films, such as a high absorption coefficient in the visible region, ambipolar charge transport, and long carrier lifetime.[2–5] The benefits of perovskites are also reflected in their ease of synthesis, that has enabled fabrication of high efficiency devices using various solution deposition techniques, such as spin coating[6], doctor-blade coating[7], slot-die coating[8] or ink-jet printing[9]. Even though solvent[6] and interfacial engineering[10] have led to more homogeneous and relatively defect-free perovskite films, a number of key issues remain. In particular, if PSCs are to be technologically and commercially viable, challenges that must be overcome include not only the inherent toxicity of the material due to the presence of lead, but more importantly, limited device life-times associated with susceptibility to ambient air and possible ion migration within the crystal lattice. Thus for PSCs to be able to generate electricity continuously, long-term stability is a necessary prerequisite, and further, the crystal structure must be stabilized in order to obtain high efficiency devices with steady output power.[11]

Efforts to address perovskite stability include approaches such as interface modification[12], dopants[13], component selection[14], and encapsulation[15], among others. For instance, Graetzel and coworkers modified the surface of $MAPbI_3$ by spin-coating its precursor solution in the presence of butylphosphonic acid 4-ammonium chloride,[16] while others used a self-assembled hydrophobic fluoroalklsilane coating on the surface of the perovskite films.[17] Very recently, it was reported that the addition of a polymer into the precursor solution, in a one-step deposition process, can tune perovskite morphology thereby enhancing device stability in air. Examples of polymers that have been explored include polyethylene glycol (PEG) [18], phenethylamine[19], polyurethane[20], *etc.* However, incorporation of these polymers into the film had a negative impact on the $MAPbI_3$ perovskite film morphology, because of steric hindrance induced by the polymer used.

Polyvinylpyrrolidone (PVP) is an alternative polymer that has been investigated in efforts to stabilize the active layer, however, the resultant perovskite films continued to have an unacceptably high number of defects.[21–23] PVP is an attractive additive because of its strong polar carbon-oxygen double bond, which is expected to interact with the perovskite precursor components and thereby stabilize the perovskite crystal structure. Here, we demonstrate how commercial PVP, coupled with optimization of the deposition parameters, provides for defect free perovskite films. PVP K-30 (M_w = 40,000 g/mol; K-value of viscosity for a 1% solution ~30) was directly introduced into the perovskite precursor solution, and through optimization of the perovskite precursor to additive ratio, was shown to facilitate formation of highly compact and uniform perovskite films, which in a device configuration exhibited efficiencies in the range of 16%. The PVP-perovskite system displayed excellent stability upon storage in ambient air (relative humidity ≥ 60%) and further, was shown to provide a platform for flexible perovskite device fabrication.

2. EXPERIMENTAL SECTION

2.1 Materials and Reagents

All materials were purchased from Sinopharm Chemical Reagent Co., Ltd. and used as received, with the exception of the following: $CH(NH_2)_2I$ (FAI), CH_3NH_3Br (MABr), and Spiro-MeOTAD (2,2',7,7'-tetrakis [N, N-di(4-methoxyphenyl) amine)-9, 9'-spirobifluorene, purity ≥ 99.5 %) were purchased from Xi'an Polymer Light Technology Corp. Fluorine doped tin oxide (FTO) coated glass (14 Ω $square^{-1}$,) and indium tin oxide (ITO) coated PET (Polyethylene terephthalate) (7 Ω $square^{-1}$) were purchased from Nippon Sheet Glass Co., Ltd. Polyvinylpyrrolidone (PVP, M_w=40,000 g/mol) was purchased from Sigma-Aldrich.

2.2 Fabrication of the Perovskite Device

FTO conductive glass was washed through sequential ultrasonic treatment in detergent, acetone, ethanol and deionized water, and was then treated in an O_2 plasma for 30 min (DT-01, Suzhou Omega Machinery Electronic Technology Co., Ltd.). Low temperature SnO_2 electron transport layers were prepared according to the method described by Chattopadhyay.[24] $SnCl_2 \cdot 2H_2O$ (22.56 mg) was dissolved in 10 ml isopropyl alcohol, and the resulting solution was stirred at reflux temperature (70 °C) for one hour and then aged for 6 h to form the sol. A volume of 50 μl of nanoparticle SnO_2 sol was spin-coated onto either an FTO glass or ITO/PET substrate, and then sintered on a hotplate at 90 °C for 3 h.

PbI_2 (507 mg, 1.1 mmol), $PbBr_2$ (73.4 mg, 0.2mmol), FAI (172 mg, 1.0 mmol), and CH_3NH_3Br (22.4 mg, 0.2 mmol) with 0-12 wt% PVP were added to 1.0 mL of dimethylformamide and dimethylsulfoxide (4:1, v/v), and the resulting mixture was stirred at 80 °C until all components were dissolved. The resulting hybrid perovskite precursor solution was spin-coated onto SnO_2/FTO or SnO_2/ITO substrates at 3000 rpm for 30 s using a one-step method. During spin-coating, the samples were washed with toluene, a non-polar solvent. The perovskite films were then annealed at 110 °C for 10 min on a hotplate while covered by a petri dish to further remove residual solvents. A spiro-OMeTAD solution (25 μL) was then spin-coated onto the as prepared perovskite film at 4000 rpm for 30 s. All operations were carried out in ambient air without controlling relative humidity. [25] Finally, the devices were coated with an 80 nm gold electrode by evaporation through an aperture mask in a vacuum chamber. The active area of the perovskite device was 0.16 cm^2.

2.3 Characterization

The perovskite film was characterized by X-ray diffraction (XRD) (Model D/max 2550V, Rigaku Co. Tokyo, Japan) by using Cu Kα (λ=1.5406 Å) radiation. The morphology of the resultant perovskite film was observed by using field-emission scanning electron microscopy (FESEM, Model S-4800, Hitachi, Japan). Tapping mode atomic force microscopy (AFM) imaging was carried out using a Multimode NanoScope IV system (Veeco, Santa Barbara, CA) at a scanning range and speed of

2μm and 3.001 Hz, respectively. Steady-state photoluminescence (PL) spectra were acquired with a FLS920 transient optical spectrometer (Edinburgh Instruments, UK). Ultraviolet photoelectron spectroscopy characterization of the PVP-perovskite film was performed using a monochromatic He I light source (21.2 eV) and a VG Scienta R4000 analyzer. The photocurrent density-voltage (J-V) curves of the PSCs were acquired using a Keithley 2400 Source Measuring Unit. A solar simulator (Model 96160 Newport Co., USA) equipped with a 300 W Xenon lamp was used as a light source, where the light intensity was adjusted using an NREL-calibrated Si solar cell with KG-1 filter for approximating the AM 1.5G one sun light intensity. The cell performance parameters, including short-circuit current density (J_{sc}), open-circuit voltage (V_{oc}), fill factor ($FF=Pmax/(J_{sc}V_{oc})$), and photoelectron conversion efficiency ($h\ (\%)=J_{sc}*V_{oc}*FF/\text{total incident energy}\times100$), were measured and calculated from the J-V characteristics. The incident-photon-to-current conversion efficiency (IPCE) spectra were measured as a function of wavelength from 300 to 800 nm using a specially designed IPCE system (Newport Co., USA). Measurement and storage of the devices were performed in ambient conditions and without encapsulation.

3. RESULTS AND DISCUSSION

3.1 PVP-Perovskite film formation

While a one-step perovskite deposition method generally leads to films comprised of large, cuboidal grains;[26] upon storage in humid (relative humidity greater than 60%) environments, the perovskite layers decompose rapidly. It was postulated that water catalyzes the decomposition of perovskite through the reversible reactions shown below:[27]

$$\left[\mathrm{CH_3NH_3{}^+PbI_3}\right]_n + \mathrm{H_2O} \rightleftarrows \left[(\mathrm{CH_3NH_3{}^+})_{n-1}(\mathrm{PbI_3})_n\right][\mathrm{H_3O^+}]+\mathrm{CH_3NH_2} \qquad (1)$$

$$\left[(\mathrm{CH_3NH_3{}^+})_{n-1}(\mathrm{PbI_3})_n\right][\mathrm{H_3O^+}] \leftrightarrows \mathrm{HI} + \mathrm{PbI_2} + \left[(\mathrm{CH_3NH_3{}^+})(\mathrm{PbI_3})_{n-1} + \mathrm{H_2O}\right] \qquad (2)$$

Here, we describe the preparation of perovskite films with not only enhanced stability, but also flexibility, under ambient conditions using PVP as an additive, coupled with optimization of the deposition parameters. PVP was selected because of its polar characteristics that derive from the carbon-oxygen double bond (carbonyl group: C=O) present on each monomer unit. The C=O group was expected to interact with other polar species present in the perovskite precursor solution through hydrogen bonding, thereby facilitating incorporation of the polymer into the active material matrix during film deposition. Mechanistically, the long chain PVP was expected to form a framework around the perovskite crystals, thus creating a barrier to moisture penetration into the inorganic lattice. In addition, incorporation of the flexible polymer might allow some latitude in bending devices fabricated on plastic substrates, thereby maintaining performance.

As evidenced by the FE-SEM surface and cross section images (**Figure 1a-1d, Figure 1i-1l,** respectively), perovskite morphology changed dramatically upon incorporation of PVP, and notably, the PVP modified layers appeared more uniform and homogeneous. As presented in **Figure 1e-1h**, the particle/grain size changed when PVP was added to the precursor solution; for 0, 4, 8 and 12 wt% PVP-perovskite films, the grain sizes were *ca.* 400 nm, 100 nm, 210 nm, and 350 nm respectively. In addition, in the presence of PVP, the perovskite films exhibited a narrower particle size distribution. While in all cases, inclusion of PVP afforded more homogeneous structures, when the concentration of PVP exceeded 12 wt%, the film appeared to develop large voids between individual perovskite grains. This is attributed to the transformation of the perovskite crystals derived from inductive effects [28] and the space location-obstruct effect [29] of PVP (*vide infra*). Atomic force microscopy (AFM) analysis (**Figure S1a-d**) provided insight into the surface roughness of as prepared films (Sq, root mean square height). Whereas the parent perovskite presented a Sq value of 19.34 nm (**Figure S1a**), that for 4.0 wt% PVP (**Figure S1b**) was only 7.96 nm, meaning that the surface was much smoother. For comparison, Sq for 8 and 12 wt % PVP-perovskite was 14.32 nm (**Figure S1c**) and 17.39 nm (**Figure S1d**), respectively. The AFM results were consistent with SEM observations.

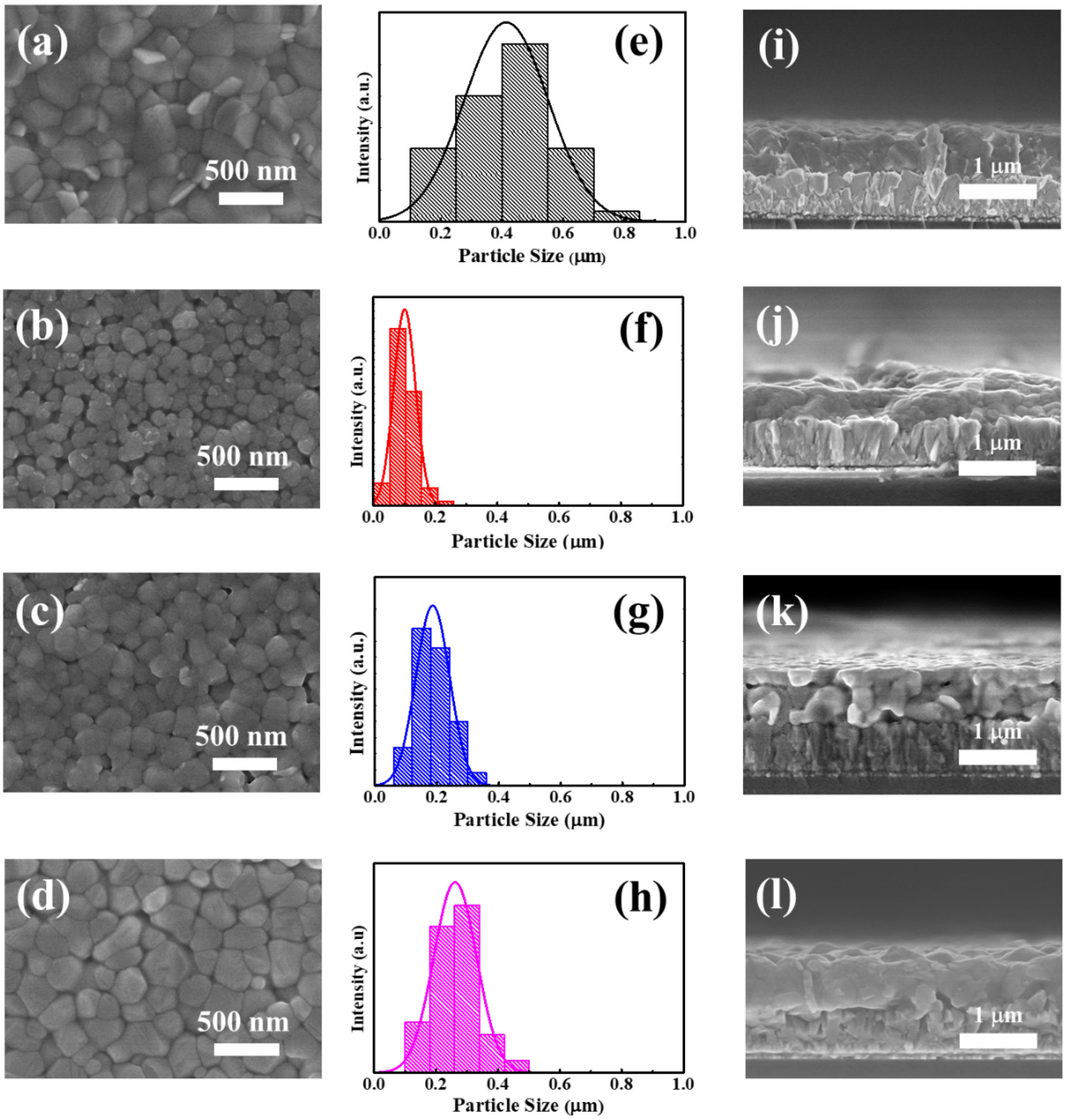

Figure 1. Surface and Cross-sectional FE-SEM image of perovskite films without PVP (a, i) and with PVP at 4 wt% (b, j), 8 wt% (c, k), and 12 wt% (d, l) concentrations. Particle size and distribution for corresponding images (e-h).

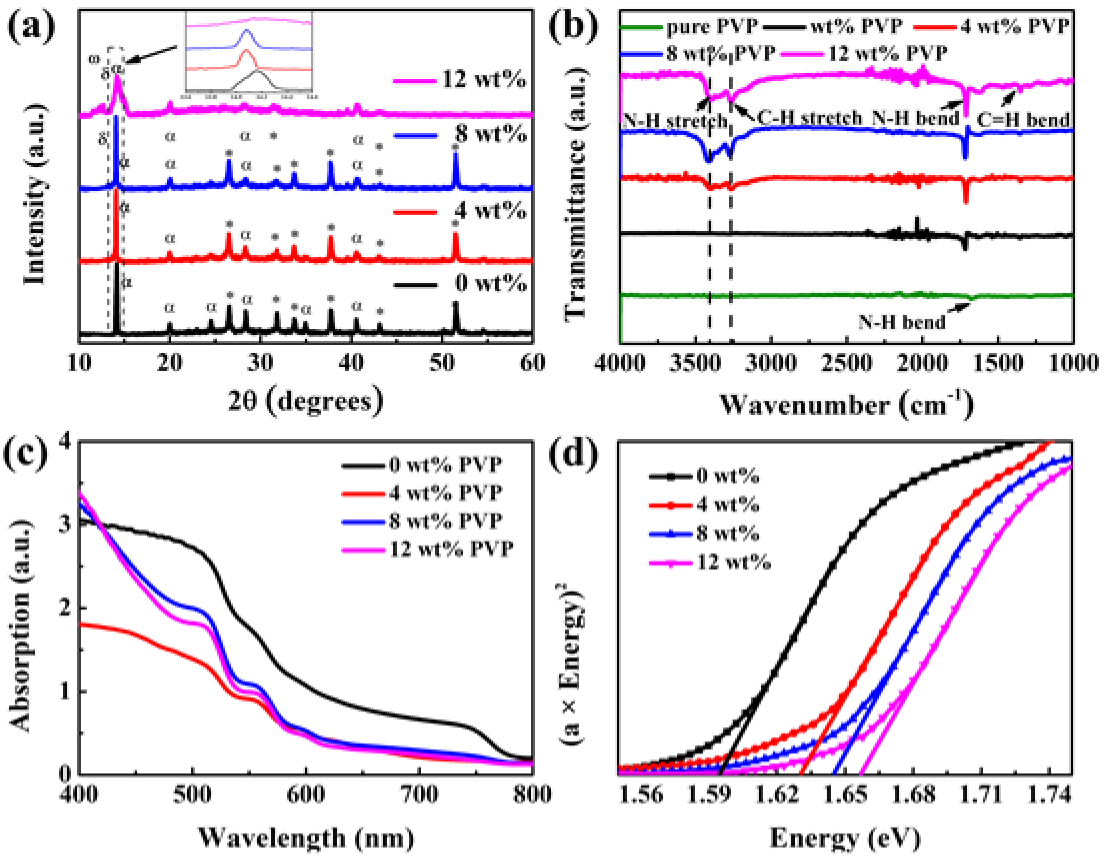

Figure 2. (a) XRD patterns of 0 wt% (black), 4 wt% (red), 8 wt% (blue), and 12 wt% (magenta) PVP-perovskite films. The diffraction peaks originating from the perovskite phase, non-perovskite phase, unreacted PbI_2 and the FTO substrate are marked by α, δ, ω, and * respectively. (b) FT-IR spectra of 0 wt% (black), 4 wt% (red), 8 wt% (blue), and 12 wt% (magenta) PVP-perovskite films, and pure PVP (green); (c) UV-Vis absorbance data of 0 wt% (black), 4 wt% (red), 8 wt% (blue), and 12 wt% (magenta) PVP-perovskite films; and (d) Tauc plots of 0 wt% (black), 4 wt% (red), 8 wt% (blue), and 12 wt% (magenta) PVP-perovskite films.

From examination of the characteristic XRD patterns presented in **Figure 2a**, 0 wt%, 4 wt%, and 8 wt% PVP-perovskite grains on FTO glass were well-crystallized, presenting signature peaks at $2\theta = 20.08°$ (200), 28.35° (220) and 40.81° (400). However, several different peaks were observed in the diffraction patterns owing to the varying PVP content. With increasing PVP concentration, the characteristic 2θ perovskite peak at 14.39° underwent a shift to a slightly lower value, as seen in the upper inset. This shift is indicative of residual stress between PVP and the perovskite crystals, which is a phenomenon found in other materials.[30] At lower PVP concentrations, this stress did not significantly influence overall film morphology. However, for PVP content above 12%, diffraction peaks attributed to residual PbI_2 and stress induced damage to the crystal structure were observed at 2θ ~12.6º (001). Conceivably, the small feature observed at 12.6° originates from the non-perovskite phase of $FAPbI_3$ that begins to form at higher concentrations of PVP. The XRD analysis is consistent with the morphologies identified by SEM (**Figure 1**): note the lighter, roughened edges of the perovskite grains in **Figure 1d**.

FT-IR spectroscopy was used to investigate the presence of chemical interactions between PVP and the perovskite. Spectra within the range of 4000-1000 cm^{-1} for pure PVP, pristine perovskite and PVP-perovskite films with varying concentrations of PVP are presented in **Figure 2b**. The higher polymer concentration sample was selected for FTIR analysis to enable identification of interactions and band shifts. The main spectral features to be considered in the pure PVP film are the tertiary amine group deformation modes at 1458 cm^{-1} and the carbonyl group vibration at 1676 cm^{-1}.[31] The C-N bending vibration appears at 1716 cm^{-1} in pristine perovskite; however, in the presence of PVP, the C-N band shifts to lower wavenumbers as the PVP concentration is increased. This observed shift may derive from interactions between perovskite C-N and PVP C=O groups. While peaks associated with C-N and N-H stretching are not obvious in the pristine perovskite film; the PVP C-H and N-H vibrational modes appear as intense bands at 3500-3000 cm^{-1} in PVP doped perovskite films. UV-Vis spectral analysis (**Figure 2c**) demonstrated that the incorporation of PVP into the perovskite layer led to a slight decrease in the absorption of visible light, where the parent perovskite exhibited the highest absorbance. The bandgap was calculated by applying Kubelka-Munk (K-M) analysis to the measured diffuse absorption spectra as follows:[32]

$$(\alpha h\nu)^2 = C(h\nu - E_g)$$

Where α represents the absorption coefficient, *h* represents Planck's constant, ν is the frequency of light, E_g is the bandgap of the material, and C is the proportionality constant - not related to E_g. The Tauc plot presented in **Figure 2d** was used to determine the perovskite bandgap as a function of PVP concentration. While the pristine perovskite bandgap was calculated to be 1.60 eV, incorporation of up to 12 wt% PVP led to a gradual increase in bandgap to 1.65 eV (**Table 1**). This change is attributed to the Pb^{2+} 4f core-level peak-shift, which dominates the perovskite bandgap.[33]

Ultraviolet photoelectron spectroscopy (UPS) was used to evaluate the effect of PVP on perovskite electronic properties. [34] Notably, incorporation of PVP led to a significant decrease in energy of the valence band (EVB) from -5.1 eV to -5.3 eV, as measured by UPS, using He(I) emission (hν =21.2 eV) as the light source (**Figure S2**). The VB edge energy (EVB) values, with reference to the vacuum level, were calculated to be -5.1 eV for the parent perovskite, and -5.2 eV, -5.3 eV and -4.6 eV for the 4, 8 and 12 wt% PVP-perovskites, respectively. The conduction band edge energies (ECB) were then determined from the E_g and EVB values; ECB for the parent was -3.5 eV, a value that is slightly deeper than that of the 4 and 8 wt% PVP-perovskite samples (-3.6 eV, -3.7eV). The incorporation of 12 wt% PVP afforded a material having an ECB value of -2.95 eV, pointing to the existence of a non-perovskite phase. In principle, the deeper perovskite conduction band could be expected to enhance charge transfer from the perovskite to the electron transport layer. [35]

Table 1. Bandgap values calculated from UV-Vis and ultraviolet photoelectron spectroscopy data.

PVP concentration (wt%)	**Bandgap (eV)**	**Valence band (eV)**	**Conduction band (eV)**
0	1.60	-5.1	-3.5
4 wt%	1.63	-5.2	-3.57
8 wt%	1.645	-5.3	-3.655
12 wt%	1.65	-4.6	-2.95

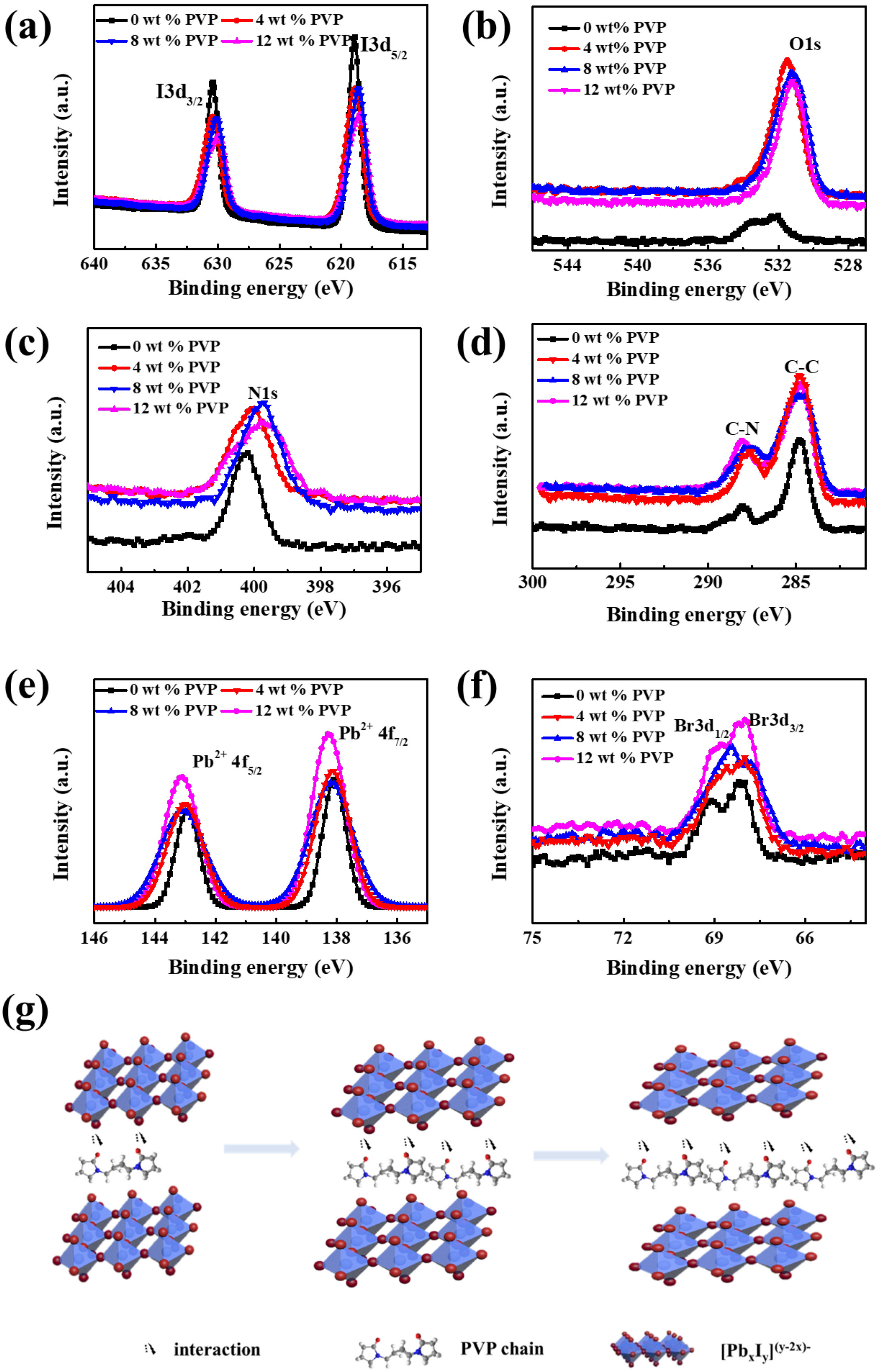

Figure 3. Core-level XPS spectra for 0 wt% (black), 4 wt% (red), 8 wt% (blue), and

12 wt% (magenta) PVP-perovskite films: (a) $I3_d$, (b) $O1_s$, (c) $N1_s$, (d) $C1_s$, (e) $Pb4_f$ and (f) $Br3_d$. (g) Schematics of the variation of perovskite crystals with PVP concentration increasing.

XPS analysis was used to further investigate the changes in binding energy of the perovskite core level peaks in the presence and absence of salt additives. The survey spectra of perovskite prepared with varying PVP concentration is presented in **Figure S3.** All of the samples were prepared on silicon substrates. All the fabricated films show nearly the same XPS peaks and intensities, indicating that the components present in all of the films are the same. The iodine, oxygen, nitrogen, carbon, lead and bromide atom binding energies are shown in **Figure 3a-f**. The spin-orbit split components of $I3_{d3/2}$ and $I3_{d5/2}$ are shifted slightly to lower energy (**Figure 3a**). The peak height of the $I3_d$ peaks (arising from the PbI_6 octahedra) decreases slightly with increasing PVP content. Abnormal deviations can also be observed in the split components of $O1_s$, $N1_s$, $C1_s$, $Pb4_f$ and $Br3_d$ (**Figure 3b-f**), all of which support the premise that the PbI_6 octahedra were disrupted by PVP chains, and is consistent with XRD analysis.

Even more remarkably, the spin-orbit split components of pristine perovskite show low strengths at 533.3 eV and 532 eV for $O1_{s2/2}$ and $O1_{s1/2}$, respectively. The peak at 533.3 eV corresponds to adsorbed molecular water.[36] With PVP doping, the peak at 533.3 eV is no longer present, which suggests that PVP serves as a barrier to protect the perovskite film from adventitious water. At the same time, the intensity of the peak near 532 eV corresponding to the C=O group has increased. Slightly shifted peaks were observed in the doped perovskite, which may derive from hydrogen bonding interactions between PVP and perovskite.[32] The experimental $Pb4_f$ signal is presented in **Figure 3e**. The spin-orbit splitting between the $Pb4_{f7/2}$ and $Pb4_{f5/2}$ lines of pristine perovskite appeared at 138.1 eV and 143 eV, respectively. However, the Pb^{2+} lines of the doped perovskite shifted to higher binding energies. The shift of the $Pb4_f$ levels can be attributed to decreased electron cloud overlap between the lead and iodide atoms, which may help account for the observed slight increase in bandgap (*vide infra*).[33]

To further explain the phenomenon, a schematic of the interactions between perovskite crystals and the PVP long chain is presented in **Figure 3g**. With increased PVP concentration, the PbI_6 octahedra become stretched. Up to a PVP concentration of about 8 wt%, the $[Pb_3I_8]^{2-}$ octahedra are able to tolerate the distortions. However, as PVP content continued to increase, the $[Pb_3I_8]^{2-}$ crystal lattice rearranged to form octahedral $[PbI_6]^{4-}$, resulting in the formation of a non-perovskite phase. The presence of $[PbI_6]^{4-}$ also impacts the absorption edge of the samples, as discussed below. [37]

Photoluminescence (PL) spectroscopy provided insightful information on the charge carrier extraction properties of solar cells fabricated from pure and PVP-containing perovskite samples. An obvious change in PL intensity was observed for PVP-perovskite films vs. the parent (**Figure S4a**). Specifically, the higher PL intensity for the 4 wt% and 8 wt% PVP-perovskite samples suggests that these films possess fewer defects. The decreased photoluminescence intensity obtained for the 12 wt% counterpart points to an increase in defect density as PVP content is increased above 8 wt%. Time-resolved PL (TRPL) spectra demonstrated that PVP content impacts photoluminescence life-time, where the 8 wt% sample exhibited a notably longer lifetime than any of the alternatives (**Figure S4b**). Combined, the PL and TRPL results suggest that at low levels (below about 8 wt%), the incorporation of PVP into the perovskite crystal structure can facilitate formation of more uniform films having fewer defects.

3.2 Device fabrication and characterization

Perovskite-based solar cells were fabricated using optimized process conditions under ambient conditions. The device architecture was comprised of either glass/FTO/compact SnO_2/perovskite/spiro-OMeTAD/Au, or PET/ITO/compact SnO_2/perovskite/spiro-OMeTAD/Au. **Figure 4a** presents a sketch of the band alignment scheme for a photovoltaic device fabricated using the hybrid active material. To avoid hysteresis, which is in part a function of the quality of the interface between the perovskite and electron transport layers, SnO_2 nanoparticles were used as the electron transport layer.[38–40] Since typically the SnO_2 nanoparticle deposition temperature is *ca.* 200 °C, a sol-gel method was developed to enable process temperatures below 185 °C in order to fabricate an SnO_2 electron transport layer suitable for plastic substrates.

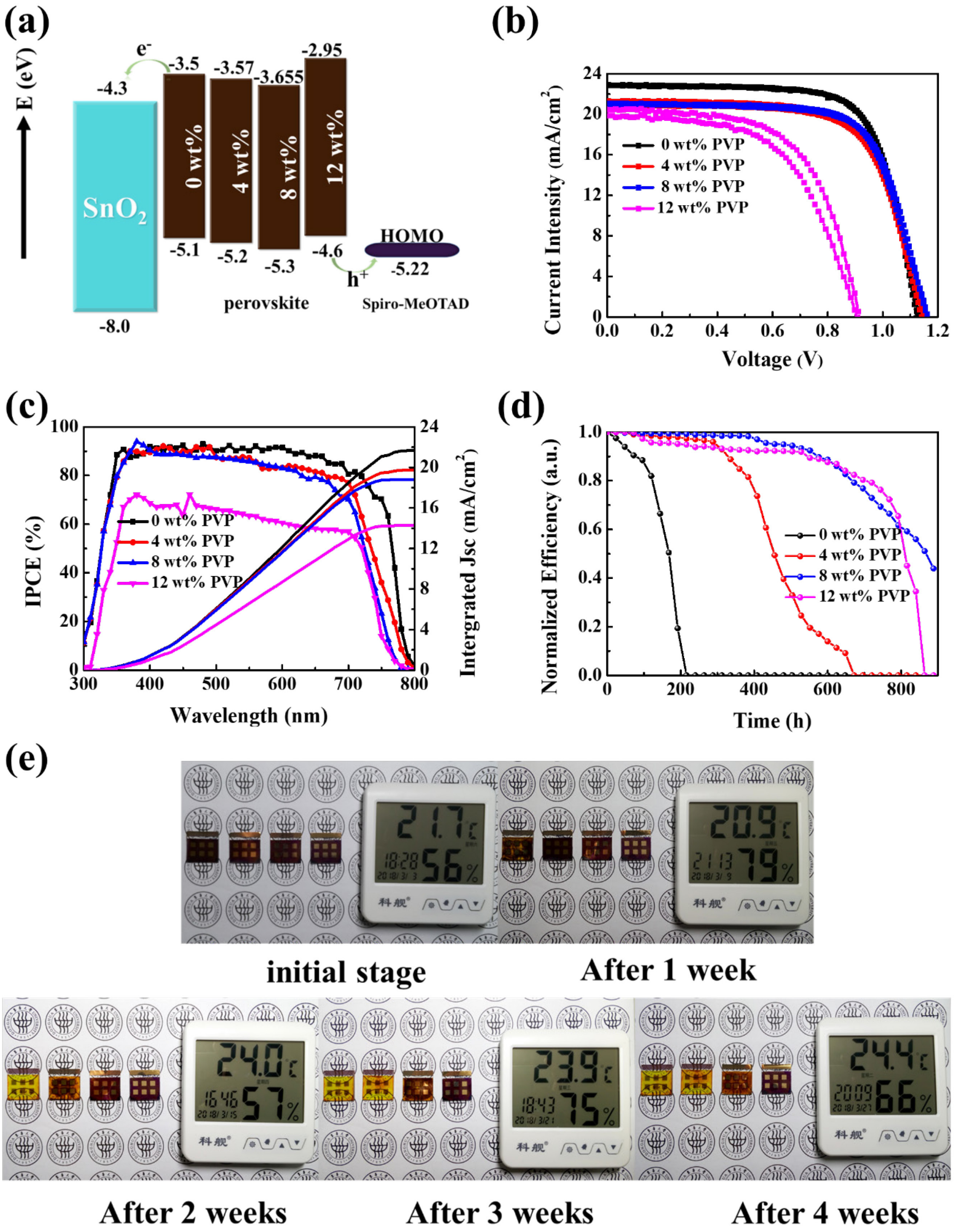

Figure 4. (a) Schematic energy level diagrams of the SnO_2 nanoparticles, 0 wt%, 4 wt%, 8 wt%, 12 wt% PVP doped perovskite and spiro-MeOTAD; (b) J−V curves of the typical devices under AM 1.5G illumination. (c) Corresponding EQE responses (left axis) and integrated current densities (right axis) of the devices containing the perovskite films with and without PVP. (d) Normalized efficiency as a factor of time; (e) Photograph of perovskite solar cell stability with varying concentrations of PVP in ambient conditions. From left to right 0 wt%, 4 wt%, 8 wt%, and 12 wt% PVP-perovskite devices.

Figure 4b presents the current-voltage curves of the pristine and PVP containing perovskite solar cells, and the data are tabulated in **Table S1**. Furthermore, statistical data regarding the photovoltaic parameters are plotted in **Figure S5**. Cells fabricated from the 0 wt%, 4 wt%, and 8 wt% PVP-perovskites exhibited little hysteresis, while significant hysteresis was observed for cells fabricated with 12 wt% PVP-perovskite. The pristine device exhibited efficiencies of 18.42 % and 18.38%, under reverse and forward scans, respectively; with corresponding V_{oc} of 1.127 V and 1.124 V, J_{sc} of 22.8 mA/cm^2 and 22.9 mA/cm^2 and FF of 71.43 % and 71.7 %. Upon incorporation of 4 wt% PVP, device efficiency in the forward and reverse directions decreased slightly to 16.7% and 16.41%, while the corresponding V_{oc}, J_{sc}, and FF values were 1.152 V and 1.141 V, 21.2 mA/cm^2 and 20.9 mA/cm^2, and 68.73 % and 68.07 %. The 8 wt% PVP-perovskite device exhibited negligible hysteresis, with an efficiency of 17.04% and 17.06%, with a V_{oc} of 1.16 V and 1.162 V, J_{sc} of 21 mA/cm^2 and 21.05 MA/cm^2, FF of 70.01 % and 69.69 % under reverse scan and forward scan, respectively. The excellent performance can be ascribed to the matched bandgap and defect-free crystals, which is in accord with the structural analysis above.

As expected from the materials characterization results, devices fabricated from 12 wt% PVP-perovskite films exhibited a significant decline in performance, namely a PCE of only 11.31 % under reverse scan and 10.18% under forward scan. V_{oc}, J_{sc} and FF were similarly negatively affected. Presumably, the low FF of 56.84 obtained for the 12 wt% PVP containing cells can be attributed to the rough perovskite morphology. It is widely believed that the key parameter associated with perovskite device performance is the FF, which may be negatively affected by carrier recombination at the interface between the perovskite and the electron/hole transport layers due to perovskite crystal degradation. [41]

Figure 4c presents the IPCE data for the devices studied here. The wavelength at which the IPCE curves experience a rapid rise is consistent with the absorption edge data discussed above: for the parent perovskite, the increase appears at around 780 nm, while for cells fabricated with 4, 8 and 12 wt% PVP-perovskite, IPCE begins to increase at about 770 nm, 760 nm and 750 nm, respectively. Between 450 nm and 700 nm, the absorption profile of devices based on pristine perovskite is higher than those of the doped perovskites, which may derive from perovskite grain size. [42] Between 350 nm and 450 nm, the absorption of the 12 wt% device decreased sharply, likely due to incomplete perovskite grain formation compared to the other three devices. [43]

Data associated with the moisture sensitivity of the perovskite devices investigated here are presented in **Figure 4d and 4e**. The parent perovskite underwent a steady decrease in efficiency from 18 % to ~1 % within 200 hours. Notably, the devices fabricated with the PVP-modified perovskite film exhibited enhanced resistance to moisture present in the ambient conditions. Incorporation of 8 wt% PVP into the perovskite layer allowed fabrication of devices that retained 80% of their original efficiency for over 600 hours under ambient conditions with 60% relative humidity. Although the initial efficiency of the 12 wt% PVP-perovskite devices is lower than the other analogs, the normalized efficiency is more stable in a humid environment, which is presumed to be directly related to protection of the perovskite by PVP.

3.3 Flexibility and bendability testing

Given the superior performance of the perovskite comprising 8 wt% PVP, that composition was used to explore the impact of the incorporation of PVP into the perovskite lattice on the flexibility of the active layer. The top-view SEM images of the parent and PVP-perovskite films fabricated on an ITO/PET substrate and subjected to mechanical bending (200 times with bending radius of 0.5 cm) are presented in **Figure 5**. The parent perovskite film (**Figure 5a**) exhibited evidence of fracturing at the grain boundaries upon bending 200 times (**Figure 5b**). In contrast, the 8 wt% PVP-perovskite films (**Figure 5c**) displayed a uniform morphology that did not appear to be compromised (**Figure 5d**). Conceivably, the incorporation of PVP into the crystalline film forms a polymer network, effectively improving the mechanical properties of the device.[20] Furthermore, steady-state PL spectra (**Figure 5e and 5f**) of the corresponding perovskite films on PET/ITO before and after bending 200 times were also analyzed. The PL intensity of the 8 wt% PVP-perovskite film (**Figure 5f**) prepared on PET/ITO was similar to that of pristine material (**Figure 5e**) prior to mechanical bending. After bending 200 times, the PVP-perovskite maintained its PL intensity, while that of the pristine film decreased. These results strongly suggest that the incorporation of PVP serves to reduce surface defects and importantly, for envisioned flexible PSC applications, instills the films with improved mechanical performance attributes.

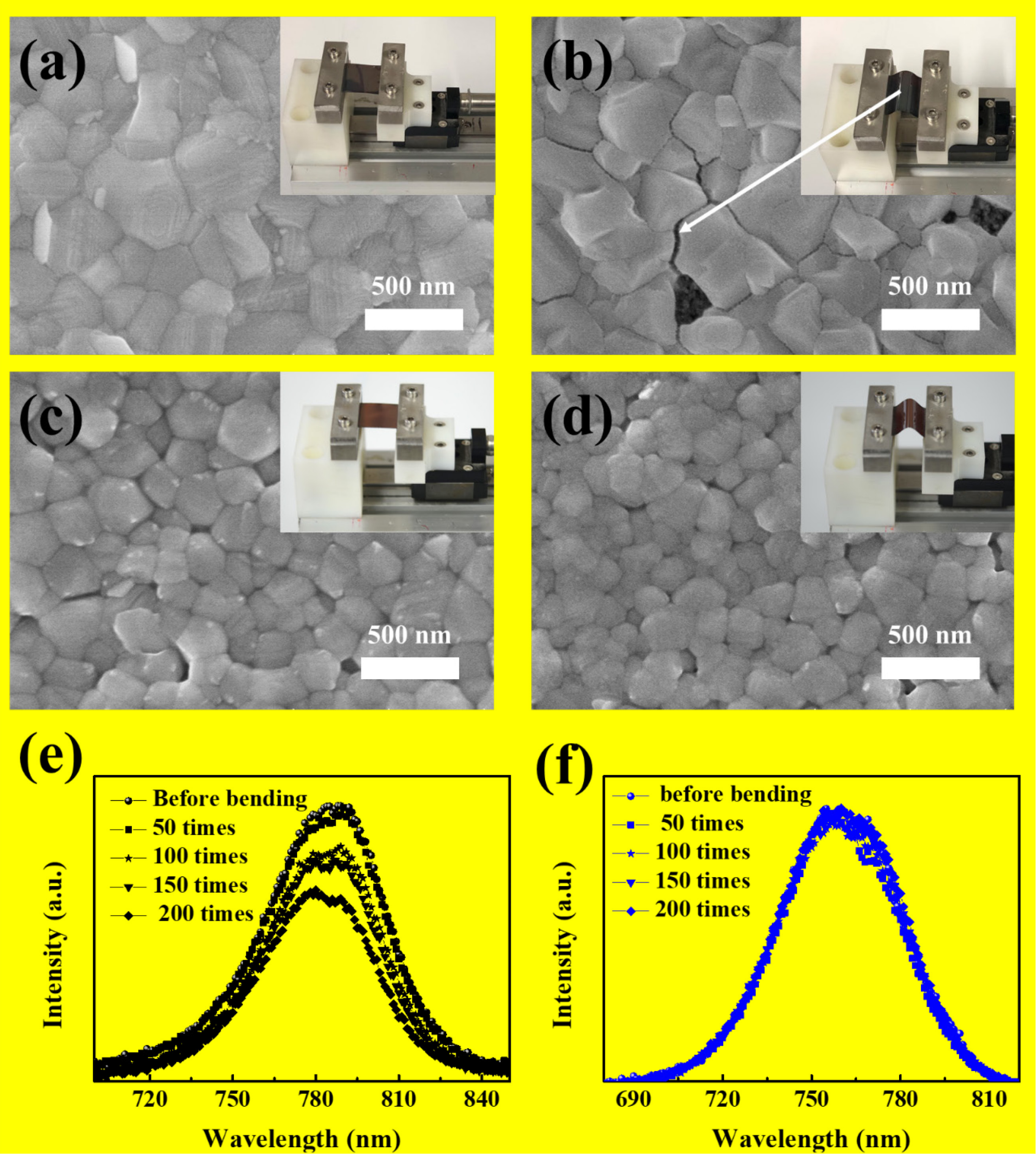

Figure 5. (a-d) Top-view SEM images of (a,b) 0 wt% PVP and (c.d) 8wt % PVP-perovskite grown on PET/ITO before and after 200 bending times with bending radius of 0.5 cm; the inset shows a photograph of the bending tests; (e)(f) steady-state PL spectra of the corresponding pristine and PVP containing perovskite films.

To further investigate the impact of PVP on the performance of the perovskite films under bending induced stress, PET/ITO/SnO_2/perovskite/spiro-MeOTAD/Au devices were fabricated and subjected to multiple bending cycles where the curvature was 5 mm for each cycle, as shown in **Figure 6.** Before bending, the PCE of PET/ITO based devices fabricated with perovskite active layers having 0 wt% and 8 wt% PVP was *ca.* 17% and *ca.* 15%, respectively. After 1000 bending cycles, the device fabricated using 8 wt% PVP-perovskite retained more than 70% of its original efficiency, whereas the pristine device exhibited less than 10% retention of its PCE. Complete data (before and after bending 1000 times) associated with flexible solar cell performance is presented in **Table S2**. Note that the V_{oc} slightly decreased in both cases; while short-circuit current decreased only slightly for the PVP containing active layer vs. the sharp decline observed when solar cell fabricated with pristine perovskite were bent 1000 times. Presumably, the decreased values of V_{oc} and J_{sc} are due to the inorganic SnO_2 film which is known to have poor flexibility. [44] The device results demonstrate that intercalation of PVP into the perovskite lattice can positively impact the mechanical properties of the hybrid active layer, allowing for the design and development of flexible devices.

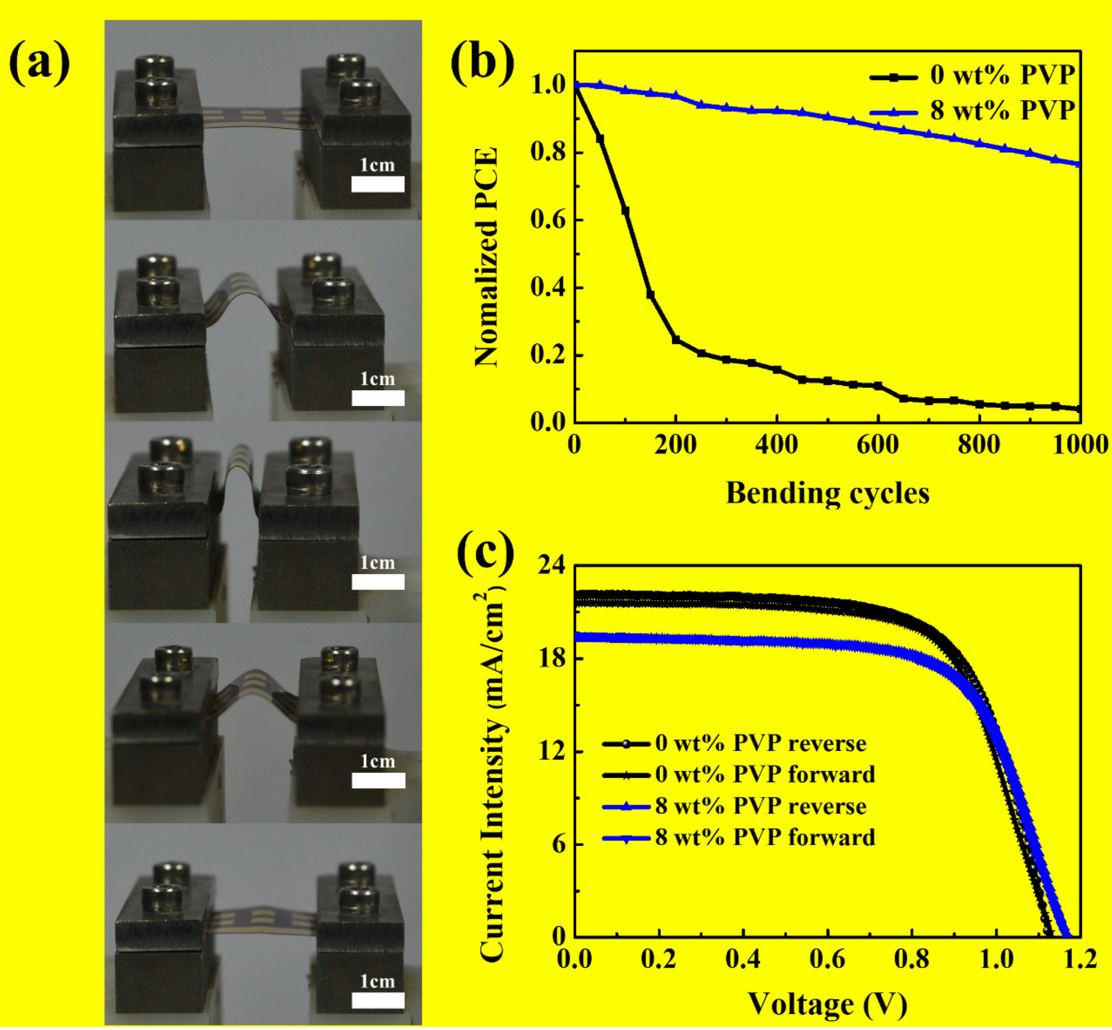

Figure 6 (a) Photograph of the bending tests for flexible devices; (b) J−V curves of 0 wt% and 8 wt% PVP-perovskite flexible devices under AM 1.5G illumination at the initial stage; (c) Mechanical stability of corresponding flexible devices.

4. CONCLUSION

In summary, polyvinylpyrrolidone was introduced into a perovskite precursor solution, and effectively integrated into the resultant perovskite film. Incorporation of the polymer was shown to both protect the active material against degradation under humid ambient conditions and impart mechanical flexibility. Mechanistically, it is believed that PVP interacts with the perovskite *via* hydrogen bonding facilitated by the presence C=O bonds along the polymer chain. The results demonstrated that with an increased proportion of PVP, perovskite crystal size increased while XRD peaks shifted slightly, which confirmed the presence of interactions between the two components. PVP-perovskite based solar cells comprising 8 wt% polymer additive exhibited a power conversion efficiency of 17%. The device efficiency remained above 15% for a duration of more than 600 hours under ambient conditions (> 60% humidity). Moreover, incorporation of PVP into the active layer facilitated fabrication of flexible solar cells, with an efficiency of *ca.* 15%, whereby the efficiencies were stable over several bending cycles. The results presented here demonstrate that polymer additives, such as PVP, that can effectively interact with the inorganic perovskite crystal can lead to environmentally stable and flexible perovskite solar cells. Modification of the perovskite through incorporation of a polymer additive is expected to enable the low-cost, large-scale fabrication of perovskite based solar cells.

ACKNOWLEDGEMENTS

We gratefully acknowledge the financial support by the Program for Professor of Special Appointment (Eastern Scholar) at Shanghai Institutions of Higher Learning , the Major Program of the National Natural Science Foundation of China (51590902). Program of Shanghai Academic Research Leader (16XD1400100), Science and

Technology Commission of Shanghai Municipality (16JC1400700), Innovation Program of Shanghai Municipal Education Commission (2017-01-07-00-03-E00055), and the Program of Introducing Talents of Discipline to Universities (No.111-2-04) are also acknowledged. We also appreciate support from the National Science Foundation, NSF EAGER 1665279. H.X. thanks the China Scholarship Council and the Fundamental Research Funds for the Central Universities (CUSF-DH-D-2017038). GD is grateful for support from the NSF EAPSI program, OISE 1613514; ER thanks the Georgia Institute of Technology for support and additionally appreciates support from the Brook Byers Institute for Sustainable Systems at Georgia Tech.

REFERENCE

[1] W.S. Yang, B.-W. Park, E.H. Jung, N.J. Jeon, Y.C. Kim, D.U. Lee, S.S. Shin, J. Seo, E.K. Kim, J.H. Noh, S. Il Seok, Iodide management in formamidinium-lead-halide–based perovskite layers for efficient solar cells, Science 356 (2017) 1376–1379.

[2] S. de Wolf, J. Holovsky, S.-J. Moon, P. Löper, B. Niesen, M. Ledinsky, F. Haug, J. Yum, C. Ballif, Organometallic Halide Perovskites: Sharp Optical Absorption Edge and, J. Phys. Chem. C. 5 (2014) 1035–139.

[3] S. Niu, H. Huyan, Y. Liu, M. Yeung, K. Ye, L. Blankemeier, T. Orvis, D. Sarkar, D.J. Singh, R. Kapadia, Bandgap Control via Structural and Chemical Tuning of Transition Metal Perovskite Chalcogenides, Adv. Mater. 29 (2017) 1604733.

[4] A. Yusoff, R. bin Mohd, H.P. Kim, X. Li, J. Kim, J. Jang, M.K. Nazeeruddin, Ambipolar Triple Cation Perovskite Field Effect Transistors and Inverters, Adv. Mater. 29 (2017) 1602940.

[5] T. Chen, W.-L. Chen, B.J. Foley, J. Lee, J.P.C. Ruff, J.Y.P. Ko, C.M. Brown, L.W. Harriger, D. Zhang, C. Park, Origin of long lifetime of band-edge charge carriers in organic–inorganic lead iodide perovskites, Proc. Natl. Acad. Sci. (2017) 201704421.

[6] N.J. Jeon, J.H. Noh, Y.C. Kim, W.S. Yang, S. Ryu, S. Il Seok, Solvent engineering for high-performance inorganic-organic hybrid perovskite solar cells., Nat. Mater. 13

(2014) 1–7.

[7] H. Back, J. Kim, G. Kim, T.K. Kim, H. Kang, J. Kong, S.H. Lee, K. Lee, Interfacial modification of hole transport layers for efficient large-area perovskite solar cells achieved via blade-coating, Sol. Energy Mater. Sol. Cells. 144 (2016) 309–315.

[8] J. Ciro, M.A. Mejía-Escobar, F. Jaramillo, Slot-die processing of flexible perovskite solar cells in ambient conditions, Sol. Energy 150 (2017) 570–576.

[9] F. Mathies, T. Abzieher, A. Hochstuhl, K. Glaser, A. Colsmann, U.W. Paetzold, G. Hernandez-Sosa, U. Lemmer, A. Quintilla, Multipass inkjet printed planar methylammonium lead iodide perovskite solar cells, J. Mater. Chem. A. 4 (2016) 19207–19213.

[10] H. Zhou, Q. Chen, G. Li, S. Luo, T. Song, H.-S. Duan, Z. Hong, J. You, Y. Liu, Y. Yang, Interface engineering of highly efficient perovskite solar cells, Science 345 (2014) 542–546.

[11] L.Q. Xie, L. Chen, Z.-A. Nan, H.-X. Lin, T. Wang, D.-P. Zhan, J.-W. Yan, B.-W. Mao, Z.-Q. Tian, Understanding the Cubic Phase Stabilization and Crystallization Kinetics in Mixed Cations and Halides Perovskite Single Crystals, J. Am. Chem. Soc. 139 (2017) 3320–3323.

[12] W. Li, W. Zhang, S. Van Reenen, R.J. Sutton, J. Fan, A.A. Haghighirad, M.B. Johnston, L. Wang, H.J. Snaith, Enhanced UV-light stability of planar heterojunction perovskite solar cells with caesium bromide interface modification, Energy Environ. Sci. 9 (2016) 490–498.

[13] J.T.W. Wang, Z. Wang, S. Pathak, W. Zhang, F. Wisnivesky-Rocca-Rivarola, J. Huang, P.K. Nayak, J.B. Patel, H.A.M. Yusof, Y. Vaynzof, Efficient perovskite solar cells by metal ion doping, Energy Environ. Sci. 9 (2016) 2892–2901.

[14] M. Saliba, T. Matsui, K. Domanski, J.-Y. Seo, A. Ummadisingu, S.M. Zakeeruddin, J.-P. Correa-Baena, W.R. Tress, A. Abate, A. Hagfeldt, M. Grätzel, Incorporation of rubidium cations into perovskite solar cells improves photovoltaic performance, Science 354 (2016) 206-209.

[15]M. Kaltenbrunner, G. Adam, E.D. Głowacki, M. Drack, R. Schwödiauer, L. Leonat, D.H. Apaydin, H. Groiss, M.C. Scharber, M.S. White, N.S. Sariciftci, S. Bauer, Flexible high power-per-weight perovskite solar cells with chromium oxide–metal contacts for improved stability in air, Nat. Mater. 14 (2015) 1032–1039.

[16]X. Li, M.I. Dar, C. Yi, J. Luo, M. Tschumi, S.M. Zakeeruddin, M.K. Nazeeruddin, H. Han, M. Grätzel, Improved performance and stability of perovskite solar cells by crystal crosslinking with alkylphosphonic acid w-ammonium chlorides, Nat. Chem. 7 (2015) 703–711.

[17]H. Xiong, Y. Rui, Y. Li, Q. Zhang, H. Wang, Hydrophobic coating over CH3NH3PbI3 absorbing layer towards air stable perovskite solar cells, J. Mater. Chem. C. 4 (2016) 6848-6854.

[18]Y. Zhao, J. Wei, H. Li, Y. Yan, W. Zhou, D. Yu, Q. Zhao, A polymer scaffold for self-healing perovskite solar cells, Nat. Commun. 7 (2016) 10228.

[19]F. Wang, W. Geng, Y. Zhou, H. Fang, C. Tong, M.A. Loi, L. Liu, N. Zhao, Phenylalkylamine Passivation of Organolead Halide Perovskites Enabling High - Efficiency and Air –Stable Photovoltaic Cells, Ad

[20]Z. Huang, X. Hu, C. Liu, L. Tan, Y. Chen, Nucleation and Crystallization Control via Polyurethane to Enhance the Bendability of Perovskite Solar Cells with Excellent Device Performance, Adv. Funct. Mater. 27 (2017) 1703061.

[21]N.A. Manshor, Q. Wali, K.K. Wong, S.K. Muzakir, A. Fakharuddin, L. Schmidt-Mende, R. Jose, Humidity versus photo-stability of metal halide perovskite films in a polymer matrix, Phys. Chem. Chem. Phys. 18 (2016) 21629–21639.

[22]Y. Guo, K. Shoyama, W. Sato, E. Nakamura, Polymer stabilization of lead (II) perovskite cubic nanocrystals for semitransparent solar cells, Adv. Energy Mater. 6 (2016) 1502317.

[23]B. Chaudhary, A. Kulkarni, A.K. Jena, M. Ikegami, Y. Udagawa, H. Kunugita, K. Ema, T. Miyasaka, Poly (4 Vinylpyridine)- Base

Voltage and Moisture Stability of Lead Halide Perovskite Solar Cells, ChemSusChem. 10 (2017) 2473–2479.

[24] A.N. Banerjee, R. Maity, S. Kundoo, K.K. Chattopadhyay, Poole–Frenkel effect in nanocrystalline SnO2: F thin films prepared by a sol–gel dip coating technique, Phys. Status Solidi. 201 (2004) 983–989.

[25] W. Nie, H. Tsai, R. Asadpour, J.-C. Blancon, A.J. Neukirch, G. Gupta, J.J. Crochet, M. Chhowalla, S. Tretiak, M.A. Alam, H.-L. Wang, A.D. Mohite, High-efficiency solution-processed perovskite solar cells with millimeter-scale grains, Science 347 (2015) 522–525.

[26] J. Frost, K. Butler, F. Brivio, Atomistic origins of high-performance in hybrid halide perovskite solar cells, Nano Lett. 14 (2014) 2584–90.

[27] A.J. Perry, V. Valvoda, D. Rafaja, X-ray residual stress measurement in TiN, ZrN and HfN films using the Seemann-Bohlin method, Thin Solid Films. 214 (1992) 169–174.

[28] J. Huang, H. Yang, M. Chen, T. Ji, Z. Hou, M. Wu, An infrared spectroscopy study of PES PVP blend and PES-g-PVP copolymer, Polym. Test. 59 (2017) 212-219.

[29] S. Liu, W. Zeng, T. Chen, Synthesis of hierarchical flower-like NiO and the influence of surfactant, Physica E. 85 (2017) 13-18.

[30] B. Gao, Y.C. Wu, Z.G. Zhang, J.J. Hua, K.D. Yao, X. Hou, Poly (acrylamide - co -acrylic acid)/Pol

Polymerization, J. Macromol. Sci. Part B Phys. 47 (2008) 544–554.

[31] B. Tripathi P. Bhatt, P.C. Kanth, P. Yadav, B. Desai, M.K. Pandey, M. Kumar, Temperature induced structural, electrical and optical changes in solution processed perovskite material: Application in photovoltaics, Sol. Energy Mater. Sol. Cells. 132 (2015) 615–622.

[32] Q. Liu, M. Qin, W. Ke, X. Zheng, Z. Chen, P. Qin, L. Xiong, H. Lei, J. Wan, J. Wen, Enhanced Stability of Perovskite Solar Cells with Low -Temperature Hydrothermally Grown SnO_2 Electron Transport Layers, Adv. Funct. Mater. 26 (2016) 6069–6075.

[33] R. Lindblad, N.K. Jena, B. Philippe, J. Oscarsson, D. Bi, A. Lindblad, S. Mandal, B. Pal, D. Das Sarma, O. Karis, Electronic structure of CH3NH3PbX3 perovskites:

dependence on the halide moiety, J. Phys. Chem. C. 119 (2015) 1818–1825.

[34] Q. Dong, Y. Shi, C. Zhang, Y. Wu, L. Wang, Energetically favored formation of SnO2 nanocrystals as electron transfer layer in perovskite solar cells with high efficiency exceeding 19%, Nano Energy. 40 (2017) 336–344.

[35] S. Ryu, J.H. Noh, N.J. Jeon, Y.C. Kim, W.S. Yang, J. Seo, S. Il Seok, Voltage output of efficient perovskite solar cells with high open-circuit voltage and fill factor, Energy Environ. Sci. 7 (2014) 2614–2618.

[36] C. Busacca, O. Di Blasi, N. Briguglio, M. Ferraro, V. Antonucci, A. Di Blasi, Electrochemical performance investigation of electrospun urchin-like V2O3-CNF composite nanostructure for vanadium redox flow battery, Electrochim. Acta. 230 (2017) 174–180.

[37] Y.C. Kim, N.J. Jeon, J.H. Noh, W.S. Yang, J. Seo, J.S. Yun, A. Ho-Baillie, S. Huang, M.A. Green, J. Seidel, Beneficial effects of PbI2 incorporated in organo-lead halide perovskite solar cells, Adv. Energy Mater. 6 (2016).

[38] K. T. Cho, S. Paek, G. Grancini, C. Roldán-Carmona, P. Gao, Y. Lee, M. K. Nazeeruddin, Highly efficient perovskite solar cells with a compositionally engineered perovskite/hole transporting material interface. Energy Environ. Sci., 10 (2017) 621–627.

[39] Q. Liu, M. C. Qin, W. J. Ke, X. L. Zheng, Z. Chen, P. L. Qin, L.B. Xiong, H.W. Lei, J.W. Wan, G. Yang, J. J. Ma, Z.Y. Zhang, G. J. Fang, Enhanced Stability of Perovskite Solar Cells with Low-Temperature Hydrothermal $_2$ Electron Transport Layers. Adv. Funct. Mater. 26 (2016) 6069–6075.

[40] Q. Jiang, L. Zhang, H. Wang, X. Yang, J. Meng, H. Liu, Z. Yin, J. Wu, X. Zhang, J. You, Enhanced electron extraction using SnO_2 for high-efficiency planar-structure $HC(NH_2)_2PbI_3$-based perovskite solar cells. Nat. Energy 2 (2016) 16177.

[41] Q. Dong, Y. Shi, C. Zhang, Y. Wu, L. Wang, Energetically favored formation of SnO_2 nanocrystals as electron transfer layer in perovskite solar cells with high efficiency exceeding 19%, Nano Energy 40 (2017) 336–344.

[42] Im, J. H., Jang, I. H., Pellet, N., Grätzel, M., & Park, N. G. (2014). Growth of

$CH_3NH_3PbI_3$ cuboids with controlled size for high-efficiency perovskite solar cells. Nature nanotechnology, 9(2014) 927-932.

[43] X. Wu, M. T. Trinh, D. Niesner, H. Zhu, Z. Norman, J. S. Owen, O.Yaffe, B. J. Kudisch, X.-Y. Zhu Trap states in lead iodide perovskites. J. Am. Chem. Soc. 137 (2015) 2089-2096.

[44] U. Ryu, S. Jee, J. Park, I. K. Han, J. H. Lee, M. Park, K. M. Choi, Nanocrystalline Titanium Metal–Organic Frameworks for Highly Efficient and Flexible Perovskite Solar Cells, ACS Nano, 12 (2018) 4968-4975

Graphic abstract For Table of Contents only